Available online at www.sciencedirect.com
SCIENCE DIRECT®
Journal of Computational Physics 197 (2004) 116–138
JOURNAL OF COMPUTATIONAL PHYSICS
www.elsevier.com/locate/jcp

Management of discontinuous reconstruction in kinetic schemes

Taku Ohwada *, Seijiro Kobayashi

Department of Aeronautics and Astronautics, Graduate School of Engineering, Kyoto University, Kyoto 606-8501, Japan

Received 7 March 2003; received in revised form 26 November 2003; accepted 26 November 2003
Available online 23 December 2003

Abstract

The present paper highlights the importance of management of the discontinuous reconstruction in the kinetic schemes for gasdynamic equation systems. Firstly, it is revealed by the analysis of the gas kinetic-BGK scheme [JCP 171 (2001) 289] that a continuous reconstruction created from a discontinuous one is a key to the successful kinetic schemes. When it is applied to a well-resolved region, the numerical flux that takes account of the collision effect correctly becomes Lax–Wendroff-like. When it is applied to an unresolved region, such as a shock layer, an appreciable numerical dissipation, which contributes to the suppression of spurious oscillations, is produced. Secondly, new kinetic schemes for the compressible Navier–Stokes (Euler) equations are developed by using the key. The numerical flux of one of the schemes is computed by using the splitting algorithm, where the effect of the molecular collision is directly taken into account and the undesirable error of the splitting algorithm in the case where the time step is much larger than the mean free time is avoided by a simple modification of the initial data. Although a discontinuous reconstruction is employed in the approximation of the initial data, the continuity is automatically taken into account in the dominant part of the numerical flux. The other schemes are the extensions of the Lax–Wendroff-type scheme to the case of the key reconstruction. Thirdly, the performance of these schemes is tested. It is demonstrated that they work as shock capturing schemes and yield fine boundary-layer profiles with a reasonable number of cells, such as 10 cells in the layer.

PACS: 65M06; 65M25; 65M15; 76P05; 76N10

Keywords: Kinetic scheme; Boltzmann equation; BGK equation; Navier–stokes equation; Euler equation; Chapman–Enskog expansion; Discontinuity

1. Introduction

A finite volume method for a macroscopic equation (system) is called kinetic if the numerical flux is computed from the solution of Cauchy problem of a kinetic equation. The equilibrium flux method

* Corresponding author. Tel.: +81-75-753-5801; fax: +81-75-753-4947.
E-mail address: ohwada@kuaero.kyoto-u.ac.jp (T. Ohwada).

0021-9991/$ - see front matter
doi:10.1016/j.jcp.2003.11.020

(EFM) for the compressible Euler equations developed by Pullin [11] is one of the origins of such schemes. It inherits the legacy of the Chapman–Enskog expansion for the Boltzmann equation; the zero-th order approximation of the distribution function (the local Maxwellian) is employed as the initial data. It also inherits the heritage of the direct simulation Monte-Carlo (DSMC) for the Boltzmann equation developed by Bird [2]. The DSMC is based on the splitting algorithm and consists of the free flow step solving the collisionless Boltzmann equation and the collision step solving the spatially homogeneous Boltzmann equation. The numerical flux of the EFM is computed from the solution of the collisionless Boltzmann equation, which corresponds to the free flow step. Then, the values of the conservative variables are updated and the new local equilibrium state is reconstructed in each cell, which corresponds to the collision step for the time step being much larger than the mean free time. Aristov and Tcheremissin extended Pullin's approach to the case of the compressible Navier–Stokes equations [1]; the initial data is changed from the local Maxwellian to the Chapman–Enskog NS distribution function (the first order approximation) but the relaxation is treated implicitly in each cell as in the case of the original Euler solver. Since this scheme employs the mesh points in the molecular velocity space, it is not efficient. This drawback was removed by Chou and Baganoff and the resulting mesh-less version is called the kinetic flux vector splitting (KFVS) scheme for the compressible Navier–Stokes equations [4]. Although Pullin's approach works very well as a shock capturing scheme, a fine viscous boundary-layer profile is never obtained with a reasonable number of cells, such as 10 cells in the layer, while the classical Lax–Wendroff scheme works very well under the same resolution. This mysterious retrogression has not attracted a lot of attention, however.

In [9,10], the senior author (T.O.) developed a method for the construction of kinetic schemes. This method, which we call the railroad method, derives the basic kinetic equation employed in the construction of the NS solvers as the kinetic equation for the Chapman–Enskog NS distribution function the macroscopic variables of which satisfy the corresponding NS equations; the relation between the resulting scheme and the macroscopic equation (NS) is direct and obvious by construction. The kinetic equation so derived has the collision term and the inclusion of the collision effect in the numerical flux contributes to the improvement of the accuracy. In fact, a kinetic solution with the collision effect yields the Lax–Wendroff-type scheme in the case of piecewise-linear reconstruction with smoothness at cell interfaces [10,13], i.e. the simple connection of cell-averaged values, and the part of the numerical flux corresponding to the collision effect removes an excess of the numerical dissipation of the splitting algorithm.

The reconstruction of the initial data that allows discontinuities at cell-interfaces is an important heritage in the CFD community and is also employed in the existing kinetic schemes, such as the KFVS scheme and Xu's gas-kinetic BGK (GKB) scheme [15]. Owing to the kinematic dissipation created by the discontinuity and the use of nonlinear limiter, they work as shock capturing schemes. While the KFVS scheme is not successful in the boundary-layer problem, the GKB scheme yields a fine boundary-layer profile with a reasonable number of cells in the layer. It is explained in [15] that this is owing to the inclusion of the collision effect in the numerical flux. As will be shown later, however, the essential reason does not lie in the inclusion of the collision effect but in the management of the discontinuous reconstruction in the evolution stage.

The present paper highlights the importance of management of the discontinuous reconstruction in the evolution stage. The organization of the paper is as follows. In Section 2, we summarize the formulas obtained by the railroad method. In Section 3, we extend the formulas to the case of discontinuous initial data straightforwardly, i.e. the simple flux splitting according to the direction of the characteristic line of the kinetic equation. It will be shown that the simple extension does not work well in the boundary-layer problem because of the kinematic dissipation created by the discontinuous reconstruction. In Section 4, we analyze the GKB scheme and reveal that a continuous reconstruction created from a discontinuous one is the essential key of the scheme. On the basis of this key, we derive new kinetic schemes. They are validated in some typical test cases. The importance of management of the discontinuous initial data becomes more

striking in the steady case, which is discussed in Section 5 together with the future extension of the present study.

2. Theory

In this section, we summarize the formulas of the railroad method for the compressible Navier–Stokes (Euler) equations [9,10].

The main notation employed in the paper is as follows. The L is the reference length of the system under consideration; ρ_0 and T_0 are the reference density and temperature; l_0 is the mean free path of the gas molecules for the equilibrium state at rest with the density ρ_0 and the temperature T_0; $\epsilon = \sqrt{\pi} l_0/(2L)$; Lx_i is the space coordinate system; $(2RT_0)^{1/2}\zeta_i$ is the molecular velocity, where R is the specific gas constant; $L(2RT_0)^{-1/2}t$ is the time; $\rho_0(2RT_0)^{-3/2}f(x_i, t, \zeta_i)$ is the distribution function of the gas molecules; $\rho_0\rho$, $(2RT_0)^{1/2}u_i$, T_0T, and P_0P ($P_0 = R\rho_0T_0$ and $P = \rho T$) are the density, flow velocity, temperature, and pressure of the gas, respectively.

For simplicity, we explain the railroad method for the compressible Navier–Stokes equations derived from the BGK equation. The nondimensional BGK equation is written as

$$\frac{\partial f}{\partial t} + \boldsymbol{\zeta}\frac{\partial f}{\partial \boldsymbol{x}} = \frac{1}{\epsilon} Q_{\mathrm{BGK}}(f), \tag{1}$$

$$Q_{\mathrm{BGK}}(f) = \rho(f_0 - f), \tag{2}$$

where f_0 is the local Maxwellian defined by

$$f_0 = \frac{\rho}{(\pi T)^{3/2}} \exp(-C^2), \tag{3}$$

$C_i = (\zeta_i - u_i)/T^{1/2}$, $C^2 = C_k^2$, and the nondimensional macroscopic variables $\boldsymbol{h} = {}^t(\rho, \rho u_1, \rho u_2, \rho u_3, 3\rho T/2 + \rho u_k^2)$ are given by

$$\boldsymbol{h} = \int \boldsymbol{\psi} f \, \mathrm{d}\boldsymbol{\zeta}, \tag{4}$$

$$\boldsymbol{\psi} = {}^t(\psi_0, \psi_1, \psi_2, \psi_3, \psi_4) = {}^t(1, \zeta_1, \zeta_2, \zeta_3, \zeta_k^2). \tag{5}$$

Eq. (1) contains the parameter ϵ, which is proportional to the ratio of the mean free path l_0 to the characteristic length L. The collision frequency of the BGK equation is given by $A_{\mathrm{c}}\rho_0\rho$, where A_{c} is a constant (it may depend on the temperature of the gas but it is treated as a constant in the present paper), and l_0 is given by $l_0 = 2\pi^{-1/2}A_{\mathrm{c}}^{-1}\rho_0^{-1}(2RT_0)^{1/2}$. The collision term Q_{BGK} satisfies the orthogonality condition:

$$\int \boldsymbol{\psi} Q_{\mathrm{BGK}}(f) \, \mathrm{d}\boldsymbol{\zeta} = 0. \tag{6}$$

The Chapman–Enskog expansion derives the distribution function in the form:

$$f(\boldsymbol{x}, t, \boldsymbol{\xi}) = f_0(\boldsymbol{h}, \boldsymbol{\xi}) + \epsilon f_1(\boldsymbol{h}, \nabla\boldsymbol{h}, \boldsymbol{\xi}) + \epsilon^2 f_2(\boldsymbol{h}, \nabla\boldsymbol{h}, \nabla^2\boldsymbol{h}, \boldsymbol{\xi}) + \cdots, \tag{7}$$

where ∇ is the abbreviation of differential operators with respect to x_i. The f_0 is the local Maxwellian and f_1 gives the viscous stress tensor and heat flow vector in the NS equation. The coefficients f_k ($k = 1, 2, \ldots$) are orthogonal to $\boldsymbol{\psi}$:

$$\int \boldsymbol{\psi} f_k \, \mathrm{d}\boldsymbol{\zeta} = 0 \quad (k = 1, 2, \ldots). \tag{8}$$

In this expansion, the conservation equations are also expanded:

$$\frac{\partial \boldsymbol{h}}{\partial t} = \boldsymbol{\Phi}_0 + \epsilon \boldsymbol{\Phi}_1 + \epsilon^2 \boldsymbol{\Phi}_2 + \cdots, \tag{9}$$

where the coefficients are given by

$$\boldsymbol{\Phi}_k = -\int \zeta_j \boldsymbol{\psi} \frac{\partial f_k}{\partial x_j} \, \mathrm{d}\boldsymbol{\zeta}. \tag{10}$$

The zero-th order approximation of the conservation equations is the compressible Euler equation system and the first order approximation is the compressible Navier–Stokes system. The explicit forms of f_1 and $\boldsymbol{\Phi}_i$ $(i = 0, 1)$ are found elsewhere, e.g. in [10].

The kinetic equation employed in the construction of NS solver is derived in the following way. Consider the distribution function

$$f(\boldsymbol{x}, t, \boldsymbol{\xi}) = f_0(\boldsymbol{h}, \boldsymbol{\xi}) + \epsilon f_1(\boldsymbol{h}, \nabla \boldsymbol{h}, \boldsymbol{\xi}), \tag{11}$$

the macroscopic variables of which satisfy the compressible NS equations

$$\frac{\partial \boldsymbol{h}}{\partial t} = \boldsymbol{\Phi}_0 + \epsilon \boldsymbol{\Phi}_1. \tag{12}$$

Substituting the above distribution function into $(\partial_t + \zeta_j \partial_{x_j}) f$ and employing Eq. (12) as the converter from the time derivative to the space derivatives, we have

$$\frac{\partial f}{\partial t} + \boldsymbol{\zeta} \frac{\partial f}{\partial \boldsymbol{x}} = \frac{\partial f_0}{\partial \boldsymbol{h}} \boldsymbol{\Phi}_0 + \boldsymbol{\zeta} \frac{\partial f_0}{\partial \boldsymbol{x}} + \epsilon \left[\frac{\partial f_0}{\partial \boldsymbol{h}} \boldsymbol{\Phi}_1 + \frac{\partial f_1}{\partial \boldsymbol{h}} \boldsymbol{\Phi}_0 + \frac{\partial f_1}{\partial \nabla \boldsymbol{h}} \nabla \boldsymbol{\Phi}_0 + \boldsymbol{\zeta} \frac{\partial f_1}{\partial \boldsymbol{x}} \right] + \epsilon^2 \left[\frac{\partial f_1}{\partial \boldsymbol{h}} \boldsymbol{\Phi}_1 + \frac{\partial f_1}{\partial \nabla \boldsymbol{h}} \nabla \boldsymbol{\Phi}_1 \right]. \tag{13}$$

Eq. (13) is nothing more than the result of computation. From now on, we regard it together with the definition of $\boldsymbol{h}$ as the evolutionary equation for f. Eq. (13) is rewritten in the form:

$$\frac{\partial f}{\partial t} + \boldsymbol{\zeta} \frac{\partial f}{\partial \boldsymbol{x}} = Q(f) = \sum_{k=0}^{2} \epsilon^k Q_k(f). \tag{14}$$

For the BGK equation, $Q_0(f)$ is given by $-\rho f_1$, i.e.

$$\frac{\partial f_0}{\partial \boldsymbol{h}} \boldsymbol{\Phi}_0 + \boldsymbol{\zeta} \frac{\partial f_0}{\partial \boldsymbol{x}} = -\rho f_1, \tag{15}$$

and $Q_1(f)$ is given by $-\rho f_2$. The collision terms $Q_k(f)$ satisfy the orthogonality condition

$$\int \boldsymbol{\psi} Q_k(f) \mathrm{d}\boldsymbol{\zeta} = 0 \quad (k = 0, 1, 2), \tag{16}$$

which follows from Eq. (8). By taking the moments of the solution of Eq. (13) from the initial data in the form of Eq. (11), we have the solution of the NS equation (12) from the macroscopic initial data corresponding to Eq. (11). Since the contribution of $Q(f)$ to $\boldsymbol{h}(\boldsymbol{x}, \Delta t)$ is $\mathrm{O}(\Delta t^2)$, we can simplify the kinetic equation. In the present study, we employ the following simplified kinetic equation

$$\frac{\partial f}{\partial t} + \boldsymbol{\zeta}\frac{\partial f}{\partial \boldsymbol{x}} = -\rho f_1. \tag{17}$$

The difference between the macroscopic variables for the solution of this simplified kinetic equation and the exact solution of the NS equation at $t = \Delta t$ is $O(\epsilon \Delta t^2)$ [10]. This is the intrinsic error of the railroad and is effectively high order for $\epsilon \lesssim \Delta t$. Incidentally, the simplified kinetic equation (17) is independent of the molecular model and the solution from the initial data in the form of $f = f_0$ constitutes the exact railroad for the compressible Euler equation.

3. Preliminary schemes

In this section, we prepare four preliminary kinetic schemes for the compressible NS (Euler) equations.

3.1. Construction of schemes

In order to avoid unessential complexity, all the following explanations are for the spatially one-dimensional case; the physical quantities are independent of x_2 and x_3. The extension to multidimensional case can be done without using any special technique and its explanation is omitted in this paper.

Multiplying Eq. (17) by $\boldsymbol{\psi}$ and integrating the result over the whole velocity space R^3, the cell $(s_{j-1/2}, s_{j+1/2})$ for x_1, and the time interval $(0, \Delta t)$, we have

$$\boldsymbol{h}_j(\Delta t) = \boldsymbol{h}_j(0) - \frac{1}{\Delta x}[\boldsymbol{F}_{j+1/2} - \boldsymbol{F}_{j-1/2}], \tag{18}$$

where $\boldsymbol{h}_j(t)$ is the average of $\boldsymbol{h}(x_1, t)$ over the cell $(s_{j-1/2}, s_{j+1/2})$, $\Delta x = s_{j+1/2} - s_{j-1/2}$, and $\boldsymbol{F}_{j+1/2}$ is the numerical flux at $x_1 = s_{j+1/2}$, which is defined by

$$\boldsymbol{F}_{j+1/2} = \int_0^{\Delta t}\int \boldsymbol{\psi}\zeta_1 f(s_{j+1/2}, t, \zeta_i)\mathrm{d}\boldsymbol{\zeta}\,\mathrm{d}t. \tag{19}$$

Since $Q_0(f)$ satisfies the orthogonality condition (16), no source term appears on the right hand side of Eq. (18).

In order to derive the formula of the numerical flux, we approximate the solution of the Cauchy problem for Eq. (17) from the initial data in the form of Eq. (11). The error of the numerical flux becomes the same order as that of the intrinsic error of the simplified railroad, $O(\epsilon \Delta t^2)$, if the approximate solution with the collision term

$$f(s_{j+1/2}, t, \boldsymbol{\zeta}) = f_0 - t\zeta_1\frac{\partial f_0}{\partial x_1} + \epsilon f_1 - t\rho f_1, \tag{20}$$

is employed, where f_0, its derivative, f_1, and ρ on the right hand side are evaluated at $(x_1, t) = (s_{j+1/2}, 0)$ (this rule will be applied to all the following formulas for f employed in the computation of the numerical flux).

The scheme becomes visible when the way of reconstruction of the initial data is specified. Here, we consider two typical reconstructions for uniform Δx. The first reconstruction is the piecewise-linear distribution with smoothness at cell interfaces (the simple connection of cell-averaged values):

Reconstruction-I

$$\boldsymbol{h}(x_1) = \begin{cases} \boldsymbol{h}_j + (\boldsymbol{h}_{j+1} - \boldsymbol{h}_j)(x_1 - s_j)/\Delta x, & \text{for } s_j \leqslant x_1 \leqslant s_{j+1/2}, \\ \boldsymbol{h}_j + (\boldsymbol{h}_j - \boldsymbol{h}_{j-1})(x_1 - s_j)/\Delta x, & \text{for } s_{j-1/2} \leqslant x_1 \leqslant s_j, \end{cases} \tag{21}$$

where s_j is the center of the cell $(s_{j-1/2}, s_{j+1/2})$. The second reconstruction is the piecewise linear distribution that allows the discontinuity at cell interfaces:

Reconstruction-II

$$\boldsymbol{h}(x_1) = \boldsymbol{h}_j + \frac{\boldsymbol{h}_{j+1} - \boldsymbol{h}_{j-1}}{2\Delta x}(x_1 - s_j) \quad (s_{j-1/2} \leqslant x_1 \leqslant s_{j+1/2}), \tag{22}$$

where the slope is computed by the central finite difference approximation. These two reconstructions are shown schematically in Fig. 1 together with Reconstruction-III, which will be introduced in Section 4. The above reconstructions can also be applied to the primitive variables ρ, u_i, and T.

We employ the superscript 'I' to express the terms at $(x_1, t) = (s_{j+1/2}, 0)$ evaluated by Reconstruction-I. Then, Eq. (20) for Reconstruction-I is written as

$$f(s_{j+1/2}, t, \boldsymbol{\zeta}) = f_0^{\mathrm{I}} - t\zeta_1 \left(\frac{\partial f_0}{\partial x_1}\right)^{\mathrm{I}} + \epsilon f_1^{\mathrm{I}} - t\rho^{\mathrm{I}} f_1^{\mathrm{I}}. \tag{23}$$

A simple way of the extension of Eq. (20) to the case of Reconstruction-II is the flux splitting according to the direction of the characteristic line (the sign of ζ_1). We employ the superscript 'II' to express the terms at $(x_1, t) = (s_{j+1/2}, 0)$ for this approximation, i.e.

$$g^{\mathrm{II}}(s_{j+1/2}, \boldsymbol{\zeta}) = g(s_{j+1/2} \mp 0, \boldsymbol{\zeta}) \quad (\text{for } \zeta_1 \gtrless 0). \tag{24}$$

Then, the simple extension of Eq. (20) to the case of Reconstruction-II is given by

$$f(s_{j+1/2}, t, \boldsymbol{\zeta}) = f_0^{\mathrm{II}} - t\zeta_1 \left(\frac{\partial f_0}{\partial x_1}\right)^{\mathrm{II}} + \epsilon f_1^{\mathrm{II}} - t\rho^{\mathrm{II}} f_1^{\mathrm{II}}, \tag{25}$$

where

$$\rho^{\mathrm{II}} = \rho(s_{j+1/2} \mp 0) \quad (\text{for } \zeta_1 \gtrless 0). \tag{26}$$

For comparison, we prepare the formula without the collision effect

$$f(s_{j+1/2}, t, \boldsymbol{\zeta}) = f_0^{\mathrm{II}} - t\zeta_1 \left(\frac{\partial f_0}{\partial x_1}\right)^{\mathrm{II}} + \epsilon f_1^{\mathrm{II}}, \tag{27}$$

and that without the collision effect and the derivative

$$f(s_{j+1/2}, t, \boldsymbol{\zeta}) = f_0^{\mathrm{II}} + \epsilon f_1^{\mathrm{II}}. \tag{28}$$

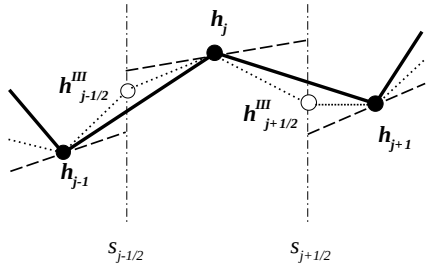

Fig. 1. The schematic figure of reconstruction. (—) Reconstruction-I, (– – –) Reconstruction-II, and (· · ·) Reconstruction-III (Section 4).

We have prepared four formulas of the kinetic solution, which are employed in the computation of the numerical flux. We will call the resulting schemes Scheme-A to Scheme-D, i.e. Scheme-A for Eq. (23), Scheme-B for Eq. (25), Scheme-C for Eq. (27), and Scheme-D for Eq. (28). Incidentally, Scheme-A is the well-known Lax–Wendroff-type scheme with the central finite difference approximation of the viscous and heat conduction terms [10] (see also [13] for the compressible Euler equations), Scheme-D is called the first order KFVS scheme, and Scheme-C is called the second order KFVS scheme.

3.2. Numerical tests of preliminary schemes

The first numerical test is the problem of structure of a normal shock wave. Fig. 2 shows the result of Scheme-D for the case where the upstream Mach number is equal to 3. The computation was carried out for $\Delta x = 0.25$ ($L = \sqrt{\pi} l_0/2$, l_0 is the mean free path of the gas molecules at upstream condition) and $\Delta t = \Delta x/50$; nonlinear limiter was not employed. Scheme-A to Scheme-D yield almost the same results, which agree very well with the standard solution of the NS equations [5]. The inclusion of the collision effect does not contribute to the improvement of the accuracy for the case where ϵ is effectively of the order of unity since the error of the numerical flux of Scheme-B becomes $O(\Delta t^2)$. This test case is for the demonstration that Scheme-A to Scheme-D are the NS solvers. Of course, the NS solution is not physically correct except for the case of weak shock, i.e. $0 < M - 1 \ll 1$, where M is the upstream Mach number; the NS solution for weak shock agrees with the solution of the Boltzmann equation only up to the order of $M - 1$ [7].

The second numerical test is done in the problem of the Blasius flow. The computational domain is the rectangle of $[-40.04 \leqslant x_1 \leqslant 107.28,\ 0 \leqslant x_2 \leqslant 29.78]$ and is divided into (120×30) cells with the minimum cell size $\Delta x_2^{\min} = 0.0252$ around $x_2 = 0$; the plate is located at $(x_2 = 0,\ 0 \leqslant x_1)$. The nonslip boundary condition is imposed at the plate surface; the specular reflection boundary condition is imposed along $(x_2 = 0,\ x_1 < 0)$; the simple inflow boundary condition is imposed at the left boundary; and the other boundary conditions (right and top) are given by the simple extrapolation. The numerical computation was carried out for the upstream Mach number $M = 0.15$ and $\epsilon = 3.2348 \times 10^{-4}$; nonlinear limiter was not employed. Incidentally, the Reynolds number Re based on the plate length in the computational domain LL_p ($L_p = 107.28$), the flow speed, and the viscosity at upstream condition, i.e. $Re = \sqrt{10/3}(ML_p/\epsilon)$, is equal to 1.02×10^5. Figs. 3–5 show the results of Scheme-A to Scheme-C for (120×30) cell system and the time step $\Delta t = 0.01$. Each component of the normalized flow velocity, $(U, V) = (u_1(x_1, \eta)/U_\infty, u_2(x_1, \eta)/u_2(x_1, \eta = \infty))$, where η is the

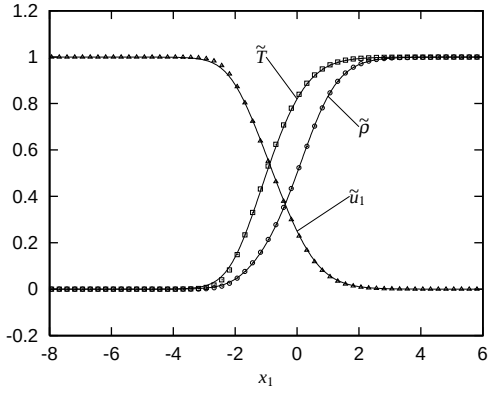

Fig. 2. The normalized density $\tilde{\rho}$, flow speed $\tilde{u}_1$, and temperature $\tilde{T}$ of the shock wave for $M = 3$. The symbols indicate the result of Scheme-D and the solid lines indicate the exact solution of the NS equations [5].

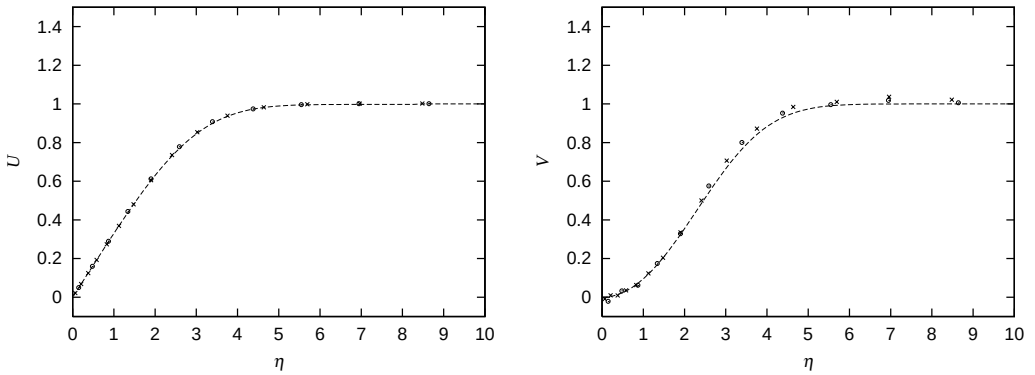

Fig. 3. Blasius flow. The results of Scheme-A for 120×30 cell system and $\Delta t = 0.01$. The dashed lines indicate the exact solutions, the symbols ○ indicate the numerical result along $x_1 = 6.436$, and the symbols × indicate that along $x_1 = 34.469$.

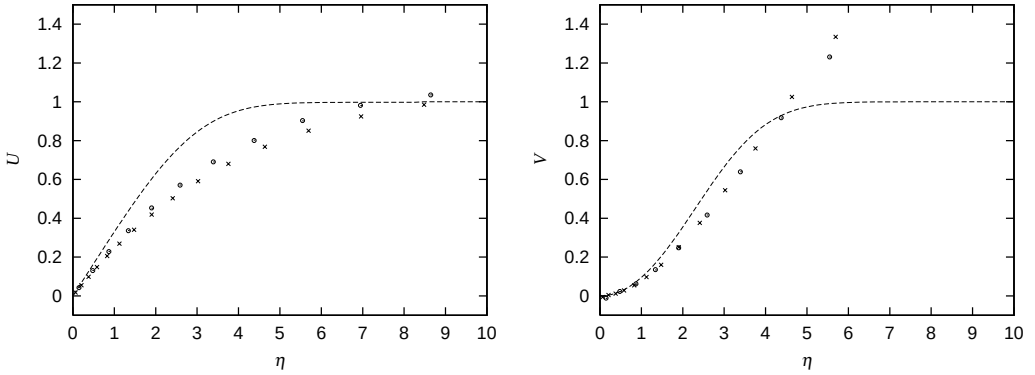

Fig. 4. Blasius flow. The results of Scheme-B for 120×30 cell system and $\Delta t = 0.01$.

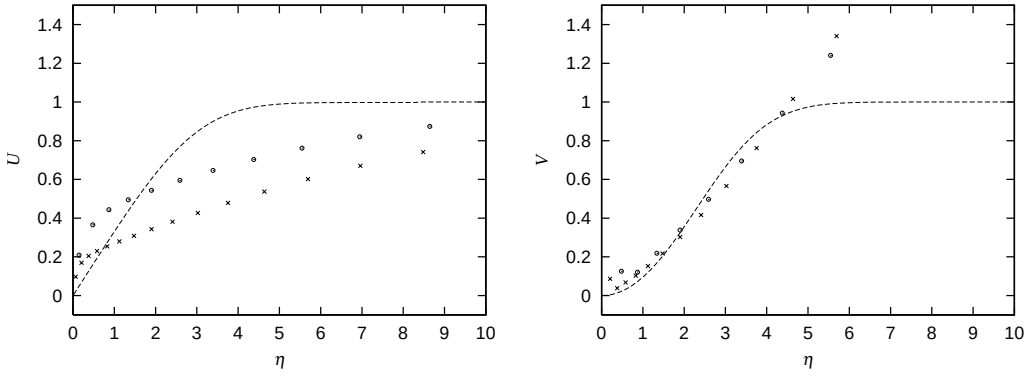

Fig. 5. Blasius flow. The results of Scheme-C for 120×30 cell system and $\Delta t = 0.01$.

similarity variable defined by $\eta = (10/3)^{1/4}(M/\epsilon)^{1/2}x_2x_1^{-1/2}$ and $U_\infty = \sqrt{5/6}M$, is plotted as a function of η. In these figures, the dashed lines indicate the exact solutions, the symbols ○ indicate the numerical result along $x_1 = 6.436$, and the symbols × indicate that along $x_1 = 34.469$; $U_\infty = 0.1369$, $u_2(x_1 = 6.436, \eta = \infty) = 1.5 \times 10^{-3}$, and $u_2(x_1 = 34.469, \eta = \infty) = 6.4 \times 10^{-4}$. While the boundary-layer profile obtained by Scheme-A (Lax–Wendroff) is excellent, those obtained by Scheme-B to Scheme-D, which employ Reconstruction-II, are very poor. Fig. 6 shows the result of Scheme-B for the finer cell system (120×120), i.e. the number of cells in the direction normal to the plate is four times larger than that of the original cell system (Δt is decreased to 0.0025 accordingly). The result of Scheme-B is greatly improved. This is not due to the decrease of dynamical dissipation; no improvement was observed for the original (120×30) cell system even if Δt is decreased. For the original (120×30) cell system, the shape of boundary-layer profile made by Reconstruction-II is sawteeth-like with deep ditches, while Reconstruction-I gives a reasonable approximation. Thus, we conclude that the discrepancy shown in Fig. 4 (Scheme-B) is due to the kinematic dissipation created by the discontinuous reconstruction. Fig. 7 shows the result of Scheme-C for the finer cell system (Δt is decreased to 0.0025 accordingly). The result is still poor. This is due to the dynamical dissipation caused by the lack of the collision effect. If the time step is further reduced, e.g. $\Delta t = 0.0001$, the result of Scheme-C finally agrees with the exact solution (no figure). Incidentally, the result of Scheme-D is

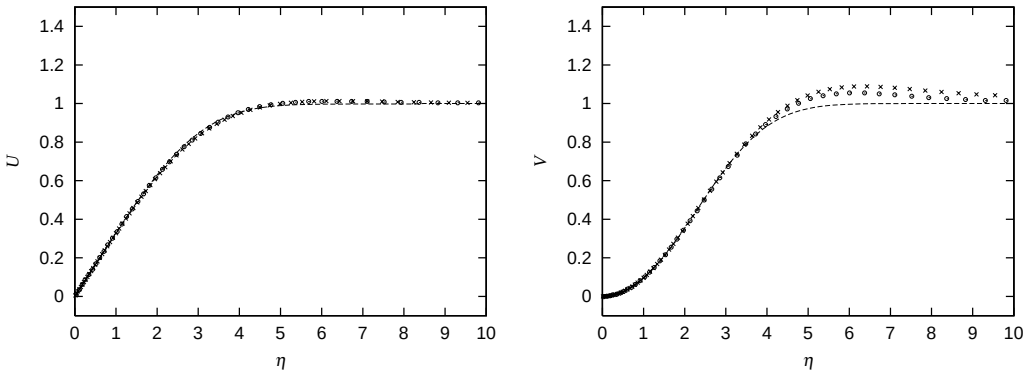

Fig. 6. Blasius flow. The results of Scheme-B for 120×120 cell system and $\Delta t = 0.0025$.

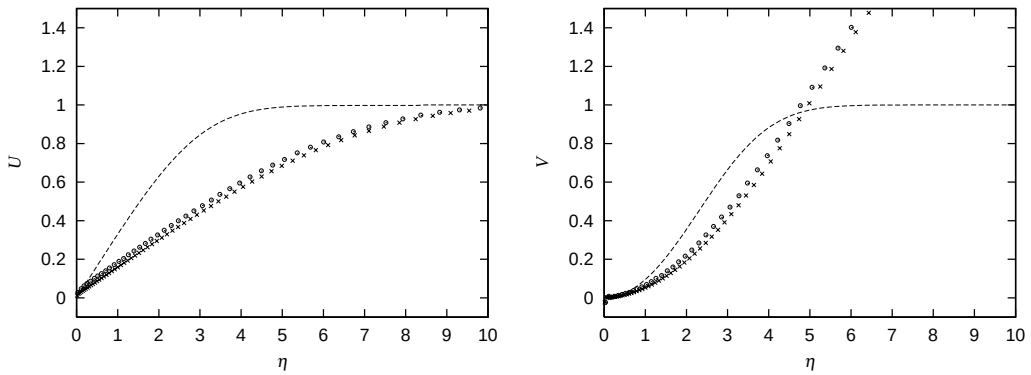

Fig. 7. Blasius flow. The results of Scheme-C for 120×120 cell system and $\Delta t = 0.0025$.

almost the same as that of Scheme-B (no figure). The reason for the mysterious reversion will be revealed in Section 5.

4. Management of discontinuity

As mentioned in Section 1, the GKB scheme works as a shock capturing scheme and yields a fine boundary-layer profile with a reasonable number of cells. In the GKB scheme, the numerical flux is computed from the solution of the BGK equation and the collision effect is explicitly taken into account there. This is in contrast to Pullin's approach, which employs the collisionless Boltzmann equation. The GKB scheme employs Reconstruction-II in the approximation of the initial data. If Reconstruction-I is employed instead of Reconstruction-II, the formula of the numerical flux coincides with Eq. (23). So, this scheme is regarded as an extension of Scheme-A to the case of discontinuous initial data. However, Xu's derivation of the scheme is not along this line and which part makes the scheme so successful in the boundary-layer problem is not obvious. In this section, we first derive the GKB scheme as an extension of Scheme-A (Section 4.1). From the analysis of numerical flux (Section 4.2), we reveal that the key lies in the management of the discontinuity. In Section 4.3, we develop new kinetic schemes using the key. The performance of these schemes is tested in Section 4.4. A promising hybrid scheme is finally proposed in Section 4.5.

4.1. Derivation of GKB scheme

Step 1 (*BGK equation with locally constant collision frequency*). In Section 3, we considered the Cauchy problem of Eq. (17) from the initial data in the form of Eq. (11) to derive the formulas of the numerical flux. As mentioned in [10], the order of intrinsic error of the scheme, i.e. $O(\epsilon\Delta t^2)$, does not change even if the BGK equation is employed instead of Eq. (17). Further, we notice that the density ρ in the collision frequency can be fixed to the value for the initial data at the cell-interface without the loss of accuracy. That is, Eq. (20) is obtained as an approximate solution of the Cauchy problem for the BGK equation with the locally constant collision frequency

$$\frac{\partial f}{\partial t} + \zeta_1 \frac{\partial f}{\partial x_1} = \frac{\rho_*}{\epsilon}(f_0 - f), \tag{29}$$

from the initial data in the form of Eq. (11). In the actual computation, the density ρ_* is evaluated at each cell interface and is updated at the beginning of each time step.

Step 2 (*Integral representation and its approximation*). The solution of the above Cauchy problem is formally expressed in the integral form of the gain term along the characteristic line:

$$\begin{aligned} f(s_{j+1/2}, t, \boldsymbol{\zeta}) = {} & \exp\left(-\frac{\rho_* t}{\epsilon}\right)[f_0(s_{j+1/2} - \zeta_1 t, 0, \boldsymbol{\zeta}) + \epsilon f_1(s_{j+1/2} - t\zeta_1, 0, \boldsymbol{\zeta})] \\ & + \frac{\rho_*}{\epsilon}\int_0^t f_0(s_{j+1/2} - \zeta_1[t-s], s, \boldsymbol{\zeta}) \exp\left(\frac{\rho_*(s-t)}{\epsilon}\right) \mathrm{d}s. \end{aligned} \tag{30}$$

The term corresponding to the initial condition and $f_0(s_{j+1/2} - \zeta_1[t-s], s, \boldsymbol{\zeta})$ in the integrand are expanded as follows:

$$f_0(s_{j+1/2} - \zeta_1 t, 0, \boldsymbol{\zeta}) + \epsilon f_1(s_{j+1/2} - \zeta_1 t, 0, \boldsymbol{\zeta}) \sim f_0 - \zeta_1 t \frac{\partial f_0}{\partial x_1} + \epsilon f_1, \tag{31}$$

$$f_0(s_{j+1/2} - \zeta_1[t-s], s, \boldsymbol{\zeta}) \sim f_0 + s\frac{\partial f_0}{\partial t} - \zeta_1(t-s)\frac{\partial f_0}{\partial x_1}. \tag{32}$$

As mentioned before, f_0, its derivatives, and f_1 on the right hand sides of Eqs. (31) and (32) are evaluated at $(x_1, t) = (s_{j+1/2}, 0)$ (the same explanation will not be repeated again). Substituting Eqs. (31) and (32) into Eq. (30) and carrying out the integration, we have

$$\begin{aligned} f(s_{j+1/2}, t, \boldsymbol{\zeta}) = {} & \exp\left(-\frac{\rho_* t}{\epsilon}\right)\left[f_0 - \zeta_1 t\frac{\partial f_0}{\partial x_1} + \epsilon f_1\right] + \left[1 - \exp\left(-\frac{\rho_* t}{\epsilon}\right)\right]\left[f_0 - \zeta_1 t\frac{\partial f_0}{\partial x_1}\right] \\ & + \left[t - \frac{\epsilon}{\rho_*}\left[1 - \exp\left(-\frac{\rho_* t}{\epsilon}\right)\right]\right]\left[\frac{\partial f_0}{\partial t} + \zeta_1\frac{\partial f_0}{\partial x_1}\right]. \end{aligned} \tag{33}$$

The time derivative of local Maxwellian at $t = 0$ is determined by the basic equation (29). The time derivative of f at $(x_1, t) = (s_{j+1/2}, 0)$ is given by

$$\frac{\partial f}{\partial t} = -\zeta_1\frac{\partial f_0}{\partial x_1} - \epsilon\zeta_1\frac{\partial f_1}{\partial x_1} - \rho_* f_1 \quad (x_1 = s_{j+1/2}, t = 0). \tag{34}$$

Taking the moments and noting Eqs. (10) and (8), we have

$$\frac{\partial \boldsymbol{h}}{\partial t} = \boldsymbol{\Phi}_0 + \epsilon\boldsymbol{\Phi}_1 \quad (x_1 = s_{j+1/2}, t = 0). \tag{35}$$

Then, we notice

$$\frac{\partial f_0}{\partial t} = \frac{\partial f_0}{\partial \boldsymbol{h}}(\boldsymbol{\Phi}_0 + \epsilon\boldsymbol{\Phi}_1) \quad (x_1 = s_{j+1/2}, t = 0). \tag{36}$$

Since the contribution of the term multiplied by ϵ in $\partial_t f_0$ becomes higher order in the numerical flux, we employ the time derivative evaluated by the Euler equations,

$$\frac{\partial f_0}{\partial t} = \frac{\partial f_0}{\partial \boldsymbol{h}}\boldsymbol{\Phi}_0 \quad (x_1 = s_{j+1/2}, t = 0). \tag{37}$$

Then, from Eq. (15), we have

$$\begin{aligned} f(s_{j+1/2}, t, \boldsymbol{\zeta}) = {} & \exp\left(-\frac{\rho_* t}{\epsilon}\right)\left[f_0 - \zeta_1 t\frac{\partial f_0}{\partial x_1} + \epsilon f_1\right] + \left[1 - \exp\left(-\frac{\rho_* t}{\epsilon}\right)\right]\left[f_0 - \zeta_1 t\frac{\partial f_0}{\partial x_1}\right] \\ & - \left[t - \frac{\epsilon}{\rho_*}\left[1 - \exp\left(-\frac{\rho_* t}{\epsilon}\right)\right]\right]\rho_* f_1. \end{aligned} \tag{38}$$

Incidentally, Eq. (37) is obtained by substituting Eq. (33) and

$$f_0(s_{j+1/2}, t, \boldsymbol{\zeta}) = f_0(s_{j+1/2}, 0, \boldsymbol{\zeta}) + t\frac{\partial f_0}{\partial t}(s_{j+1/2}, 0, \boldsymbol{\zeta}), \tag{39}$$

into Eq. (6), as done in [13] for the case of compressible Euler equations.

Step 3 (*Introduction of discontinuity*). We notice that Eq. (38) is equivalent to Eq. (20). This is the consequence of Step 1. However, Step 2 is not useless. The expression (38) suggests a guideline on the extension to the case of the discontinuous initial data. We notice that the first term on the right hand side of Eq. (38) comes from the initial data and the second and third terms come from the gain term of the BGK equation.

If we apply Reconstruction-I to all the terms, we have Scheme-A, i.e. the Lax–Wendroff-type scheme with central finite difference approximation of the viscous stress term and heat flow term. If we apply the simple flux splitting to all the terms, we have Eq. (25), i.e. Scheme-B. Now, we retain the smoothness of the gain term. Employing Reconstruction-II for the first term and Reconstruction-I for the second and third terms, we have

$$(s_{j+1/2},t,\boldsymbol{\zeta}) = \exp\left(-\frac{\rho_* t}{\epsilon}\right)\left[f_0^{\mathrm{II}} - t\zeta_1\left(\frac{\partial f_0}{\partial x_1}\right)^{\mathrm{II}} + \epsilon f_1^{\mathrm{II}}\right] + \left[1-\exp\left(-\frac{\rho_* t}{\epsilon}\right)\right]\left[f_0^{\mathrm{I}} - \zeta_1 t\left(\frac{\partial f_0}{\partial x_1}\right)^{\mathrm{I}}\right] - \left[t - \frac{\epsilon}{\rho_*}\left[1-\exp\left(-\frac{\rho_* t}{\epsilon}\right)\right]\right]\rho_* f_1^{\mathrm{I}}. \tag{40}$$

Hereafter, we will call the scheme for Eq. (40) Scheme-E. Incidentally, ρ_* can be computed from f_0^{I}, i.e. $\rho_* = \rho^{\mathrm{I}}$, or from f_0^{II}. In Scheme-E, we adopt $\rho_* = \rho^{\mathrm{I}}$.

Step 4 (*Modification of Scheme-E*). The GKB scheme is derived as a variant of Scheme-E. Xu approximated the second and third terms on the right hand side of Eq. (33) using the following reconstruction.

Reconstruction-III

$$\boldsymbol{h}(x_1) = \begin{cases} \boldsymbol{h}_j + 2(\boldsymbol{h}^{\mathrm{III}}_{j+1/2} - \boldsymbol{h}_j)(x_1 - s_j)/\Delta x, & \text{for } s_j \leqslant x_1 \leqslant s_{j+1/2}, \\ \boldsymbol{h}_j + 2(\boldsymbol{h}_j - \boldsymbol{h}^{\mathrm{III}}_{j-1/2})(x_1 - s_j)/\Delta x, & \text{for } s_{j-1/2} \leqslant x_1 \leqslant s_j, \end{cases} \tag{41}$$

where

$$\boldsymbol{h}^{\mathrm{III}}_{j+1/2} = \int \boldsymbol{\psi} f_0^{\mathrm{II}}\,\mathrm{d}\boldsymbol{\zeta}. \tag{42}$$

This reconstruction has already been shown schematically in Fig. 1. In order to express the formula of GKB scheme, we introduce the functions defined by

$$f_0^{\mathrm{III}} = f_0(\boldsymbol{h}^{\mathrm{III}}_{j+1/2}, \boldsymbol{\zeta}), \tag{43}$$

$$\left(\frac{\partial f_0}{\partial x_1}\right)^{\mathrm{III}} = \begin{cases} \frac{2(\boldsymbol{h}^{\mathrm{III}}_{j+1/2} - \boldsymbol{h}_j)}{\Delta x}\frac{\partial f_0}{\partial \boldsymbol{h}}(\boldsymbol{h}^{\mathrm{III}}_{j+1/2}, \boldsymbol{\zeta}), & \text{for } \zeta_1 > 0, \\ \frac{2(\boldsymbol{h}_{j+1} - \boldsymbol{h}^{\mathrm{III}}_{j+1/2})}{\Delta x}\frac{\partial f_0}{\partial \boldsymbol{h}}(\boldsymbol{h}^{\mathrm{III}}_{j+1/2}, \boldsymbol{\zeta}), & \text{for } \zeta_1 < 0, \end{cases} \tag{44}$$

$$f_1^{\mathrm{III}} = \begin{cases} f_1(\boldsymbol{h}^{\mathrm{III}}_{j+1/2}, 2[\boldsymbol{h}^{\mathrm{III}}_{j+1/2} - \boldsymbol{h}_j]/\Delta x, \boldsymbol{\zeta}), & \text{for } \zeta_1 > 0, \\ f_1(\boldsymbol{h}^{\mathrm{III}}_{j+1/2}, 2[\boldsymbol{h}_{j+1} - \boldsymbol{h}^{\mathrm{III}}_{j+1/2}]/\Delta x, \boldsymbol{\zeta}), & \text{for } \zeta_1 < 0. \end{cases} \tag{45}$$

Further, the density at the cell interface, ρ_*, is computed as ρ^{III} defined by

$$\rho^{\mathrm{III}} = \int f_0^{\mathrm{II}}\,\mathrm{d}\boldsymbol{\zeta}. \tag{46}$$

Then, Eq. (33) becomes

$$f(s_{j+1/2},t,\boldsymbol{\zeta}) = \exp\left(-\frac{\rho^{\mathrm{III}}t}{\epsilon}\right)\left[f_0^{\mathrm{II}} - t\zeta_1\left(\frac{\partial f_0}{\partial x_1}\right)^{\mathrm{II}} + \epsilon f_1^{\mathrm{II}}\right] + \left[1-\exp\left(-\frac{\rho^{\mathrm{III}}t}{\epsilon}\right)\right] \times \left[f_0^{\mathrm{III}} - t\zeta_1\left(\frac{\partial f_0}{\partial x_1}\right)^{\mathrm{III}}\right] + \left[t - \frac{\epsilon}{\rho^{\mathrm{III}}}\left[1-\exp\left(-\frac{\rho^{\mathrm{III}}t}{\epsilon}\right)\right]\right]\left[\frac{\partial f_0}{\partial t} + \zeta_1\left(\frac{\partial f_0}{\partial x_1}\right)^{\mathrm{III}}\right]. \tag{47}$$

In Eq. (47), the time derivative of the local Maxwellian has not yet been determined. As mentioned before, it can be determined by making use of the orthogonality of the collision term in principle. However, two different reconstructions are employed in Eq. (47) and the time derivative cannot be determined by Eq. (6). Then, Xu introduced the averaged orthogonality condition:

$$\int_0^{\Delta t}\int \boldsymbol{\psi}(f_0 - f)\mathrm{d}\boldsymbol{\zeta}\,\mathrm{d}t = 0, \tag{48}$$

where f is given by Eq. (47) and f_0 is given by

$$f_0 = f_0^{\mathrm{III}} + t\frac{\partial f_0}{\partial t}. \tag{49}$$

Since the formula of $\partial_t f_0$ is easily obtained, it is omitted here. Incidentally, the averaged orthogonality condition leads to Eq. (37) for the continuous initial data. In the actual computation of the GKB scheme, $\tau(=\epsilon/\rho_*)$ is determined by the relation between the viscosity and pressure under the modification that takes account of the pressure jump [15]. In the present paper, the GKB scheme means its simplest version, i.e. $\tau = \epsilon/\rho^{\mathrm{III}}$.

In the derivation of Scheme-E, we employed Eq. (15) and did not employ the orthogonality condition (6). Similar to this derivation, we can bypass the time averaging procedure by replacing $\partial_t f_0 + \zeta_1(\partial_{x_1} f_0)^{\mathrm{III}}$ [the third term on the right hand side of Eq. (47)] with $-\rho^{\mathrm{III}} f_1^{\mathrm{III}}$. We call the resulting scheme the modified GKB scheme.

4.2. Analysis of numerical flux

In this subsection, we analyze the numerical flux of Scheme-E and that of the GKB scheme. For this purpose, we introduce the functional defined by

$$\mathscr{F}[g] = \int \zeta_1 \boldsymbol{\psi} g\,\mathrm{d}\boldsymbol{\zeta}. \tag{50}$$

Before proceeding to the analysis, we list the numerical fluxes of Scheme-A to Scheme-D, $\boldsymbol{F}_{\mathrm{A}}$ to $\boldsymbol{F}_{\mathrm{D}}$, below:

$$\boldsymbol{F}_{\mathrm{A}} = \Delta t\mathscr{F}[f_0^{\mathrm{I}}] + \epsilon\Delta t\mathscr{F}[f_1^{\mathrm{I}}] - \frac{\Delta t^2}{2}\mathscr{F}\left[\zeta_1\left(\frac{\partial f_0}{\partial x_1}\right)^{\mathrm{I}}\right] - \frac{\Delta t^2}{2}\mathscr{F}[\rho^{\mathrm{I}} f_1^{\mathrm{I}}], \tag{51}$$

$$\boldsymbol{F}_{\mathrm{B}} = \Delta t\mathscr{F}[f_0^{\mathrm{II}}] + \epsilon\Delta t\mathscr{F}[f_1^{\mathrm{II}}] - \frac{\Delta t^2}{2}\mathscr{F}\left[\zeta_1\left(\frac{\partial f_0}{\partial x_1}\right)^{\mathrm{II}}\right] - \frac{\Delta t^2}{2}\mathscr{F}[\rho^{\mathrm{II}} f_1^{\mathrm{II}}], \tag{52}$$

$$\boldsymbol{F}_{\mathrm{C}} = \Delta t\mathscr{F}[f_0^{\mathrm{II}}] + \epsilon\Delta t\mathscr{F}[f_1^{\mathrm{II}}] - \frac{\Delta t^2}{2}\mathscr{F}\left[\zeta_1\left(\frac{\partial f_0}{\partial x_1}\right)^{\mathrm{II}}\right]. \tag{53}$$

$$\boldsymbol{F}_{\mathrm{D}} = \Delta t \boldsymbol{\mathscr{F}}[f_0^{\mathrm{II}}] + \epsilon \Delta t \boldsymbol{\mathscr{F}}[f_1^{\mathrm{II}}]. \tag{54}$$

The expression of the numerical flux of Scheme-E, $\boldsymbol{F}_{\mathrm{E}}$, and that of the GKB scheme, $\boldsymbol{F}_{\mathrm{GKB}}$, are a little bit lengthy and we show them in the following two limiting cases. For $\Delta t \ll \epsilon$, $\boldsymbol{F}_{\mathrm{E}}$ and $\boldsymbol{F}_{\mathrm{GKB}}$ become

$$\boldsymbol{F}_{\mathrm{E}} \sim \boldsymbol{F}_{\mathrm{GKB}} \sim \boldsymbol{F}_{\mathrm{D}}, \tag{55}$$

where the higher order terms with respect to Δt are omitted in this limiting case (the same explanation will not be repeated). That is, these schemes behave like the KFVS scheme. For $\epsilon \ll \Delta t$, $\boldsymbol{F}_{\mathrm{E}}$ becomes

$$\boldsymbol{F}_{\mathrm{E}} \sim \boldsymbol{F}_{\mathrm{A}} + \frac{\epsilon}{\rho^{\mathrm{I}}} \boldsymbol{\mathscr{F}}[f_0^{\mathrm{II}} - f_0^{\mathrm{I}}], \tag{56}$$

where the higher order terms with respect to ϵ are omitted in this limiting case (the same explanation will not be repeated). Scheme-E becomes the Lax–Wendroff-type scheme for the compressible Euler equations in the limit of $\epsilon = 0$. Therefore, it is not shock capturing and is excluded from the list of candidates for robust kinetic schemes. The numerical flux $\boldsymbol{F}_{\mathrm{GKB}}$ for $\epsilon \ll \Delta t$ is evaluated in the following way. By noting $\int \boldsymbol{\psi}(f_0^{\mathrm{II}} - f_0^{\mathrm{III}})\mathrm{d}\boldsymbol{\zeta} = 0$, we notice that the time derivative $\partial_t f_0$ in Eq. (47) becomes

$$\frac{\partial f_0}{\partial t} \sim \frac{\partial f_0}{\partial \boldsymbol{h}}(\boldsymbol{h}_{j+1/2}^{\mathrm{III}}, \boldsymbol{\zeta}) \Delta \boldsymbol{h}^{\mathrm{III}}, \tag{57}$$

where

$$\Delta \boldsymbol{h}^{\mathrm{III}} = -\int \zeta_1 \boldsymbol{\psi} \left(\frac{\partial f_0}{\partial x_1} \right)^{\mathrm{III}} \mathrm{d}\boldsymbol{\zeta}. \tag{58}$$

Then, we have

$$\begin{aligned} \boldsymbol{F}_{\mathrm{GKB}} \sim{}& \Delta t \boldsymbol{\mathscr{F}}[f_0^{\mathrm{III}}] - \frac{\Delta t^2}{2} \boldsymbol{\mathscr{F}} \left[\zeta_1 \left(\frac{\partial f_0}{\partial x_1} \right)^{\mathrm{III}} \right] + \left(\frac{\Delta t^2}{2} - \frac{\epsilon \Delta t}{\rho^{\mathrm{III}}} \right) \left(\boldsymbol{K} \Delta \boldsymbol{h}^{\mathrm{III}} + \boldsymbol{\mathscr{F}} \left[\zeta_1 \left(\frac{\partial f_0}{\partial x_1} \right)^{\mathrm{III}} \right] \right) \\ &+ \frac{\epsilon}{\rho^{\mathrm{III}}} \boldsymbol{\mathscr{F}}[f_0^{\mathrm{II}} - f_0^{\mathrm{III}}], \end{aligned} \tag{59}$$

where $\boldsymbol{K}$ is the matrix whose elements K_{ij} are defined by

$$K_{ij} = \int \zeta_1 \psi_i \frac{\partial f_0}{\partial h_j}(\boldsymbol{h}_{j+1/2}^{\mathrm{III}}, \boldsymbol{\zeta}) \mathrm{d}\boldsymbol{\zeta}. \tag{60}$$

We notice that $\Delta \boldsymbol{h}^{\mathrm{III}}$ corresponds to $\boldsymbol{\Phi}_0$ [see Eq. (10)] and $\boldsymbol{K}\Delta \boldsymbol{h}^{\mathrm{III}}$ corresponds to the numerical flux for $(\partial f_0/\partial \boldsymbol{h})\boldsymbol{\Phi}_0$. From Eq. (15), we notice that the third term on the right hand side of Eq. (59) corresponds to $\epsilon \Delta t \boldsymbol{\mathscr{F}}[f_1] - (\Delta t^2/2)\boldsymbol{\mathscr{F}}[\rho f_1]$. The influence of Reconstruction-II survives only in the fourth term, which is $\mathrm{O}(\epsilon)$ and is much smaller than Δt. Thus, we conclude that the GKB scheme for $\epsilon \ll \Delta t$ is an extension of Scheme-A to the case of Reconstruction-III. Then, the reason why the GKB scheme works like Scheme-A in the Blasius flow problem becomes obvious if Reconstruction-III is shown to yield an approximation that is nearly equivalent to that of Reconstruction-I in a resolved region, which will be demonstrated in Section 4.4. Incidentally, the contribution of ϵf_1 in the initial condition to the numerical flux is $\mathrm{O}(\epsilon^2)$ for $\epsilon \ll \Delta t$; the initial condition in the form of $f = f_0$ suffices. This gives the theoretical legitimacy of the previous version of GKB scheme [14].

Finally, we show the numerical flux of the modified GKB scheme, $\boldsymbol{F}_{\mathrm{MGKB}}$, for the above two limiting cases. For $\Delta t \ll \epsilon$, it is evaluated as $\boldsymbol{F}_{\mathrm{MGKB}} \sim \boldsymbol{F}_{\mathrm{D}}$. For $\epsilon \ll \Delta t$, it is evaluated as

$$\boldsymbol{F}_{\mathrm{MGKB}} \sim \Delta t \mathscr{F}[f_0^{\mathrm{III}}] + \epsilon \Delta t \mathscr{F}[f_1^{\mathrm{III}}] - \frac{\Delta t^2}{2} \mathscr{F}\left[\zeta_1 \left(\frac{\partial f_0}{\partial x_1}\right)^{\mathrm{III}}\right] - \frac{\Delta t^2}{2} \mathscr{F}[\rho^{\mathrm{III}} f_1^{\mathrm{III}}] + \frac{\epsilon}{\rho^{\mathrm{III}}} \mathscr{F}[f_0^{\mathrm{II}} - f_0^{\mathrm{III}}] \tag{61}$$

[cf. Eq. (56)].

4.3. New kinetic schemes

In this subsection, we derive new kinetic schemes making use of the key revealed by the analysis of the GKB scheme in the previous subsection. We first derive a scheme on the basis of the Cauchy problem for the BGK equation with the locally constant collision frequency (29) from the initial data in the form of the Chapman–Enskog NS distribution function, which is the same starting point as that of the derivation of the GKB scheme. Instead of the integral form of the BGK equation (30), we employ the splitting algorithm as the BGK solver. This is different usage of the splitting algorithm from Pullin's approach; the splitting algorithm is directly applied to the computation of the numerical flux and the effect of the molecular collision is explicitly taken into account. Although Reconstruction-II is employed in the approximation of the initial data, the gain term is automatically approximated by Reconstruction-III. However, the error of the splitting algorithm becomes larger than the intrinsic error of the Cauchy problem for $\epsilon \ll \Delta t$. This drawback is overcome by a simple modification of the initial data under the guideline of the railroad method in Section 2.

We derive the formula of the numerical flux at the cell interface $x_1 = s_{j+1/2}$. Similar to the derivation of the GKB scheme, we start with the BGK equation with the locally constant collision frequency, Eq. (29). However, we modify the initial data slightly:

$$f = f_0 + \beta f_1, \tag{62}$$

where β is an undetermined constant and is assumed to be of the order of ϵ or Δt. The formula of β is obtained in the following analysis in the case of smooth initial data.

The splitting algorithm for the BGK equation consists of the free flow step solving the collisionless Boltzmann equation,

$$\frac{\partial f}{\partial t} + \zeta_1 \frac{\partial f}{\partial x_1} = 0, \tag{63}$$

and the collision step solving the spatially homogeneous BGK equation,

$$\frac{\partial f}{\partial t} = \frac{\rho_*}{\epsilon}(f_0 - f). \tag{64}$$

There are two choices concerning the order of the steps in the splitting algorithm; we can carry out the collision step after the free flow step, and vice versa. Here, we carry out the free flow step first. Then, the exact result of the splitting algorithm is expressed as

$$f(s_{j+1/2}, t, \boldsymbol{\zeta}) = \exp\left(-\frac{\rho_* t}{\epsilon}\right) f_{\mathrm{F}} + \left[1 - \exp\left(-\frac{\rho_* t}{\epsilon}\right)\right] \mathscr{M}(f_{\mathrm{F}}), \tag{65}$$

where f_{F} is the solution of the collisionless Boltzmann equation,

$$f_{\mathrm{F}} = f_0(s_{j+1/2} - \zeta_1 t, 0, \boldsymbol{\zeta}) + \beta f_1(s_{j+1/2} - \zeta_1 t, 0, \boldsymbol{\zeta}), \tag{66}$$

and $\mathscr{M}(g)$ is the Maxwellian generated from g, i.e.

$$\mathscr{M}(g) = f_0(\boldsymbol{h}_g, \boldsymbol{\zeta}), \tag{67}$$

$$\boldsymbol{h}_g = \int \boldsymbol{\psi} g \, \mathrm{d}\boldsymbol{\zeta}. \tag{68}$$

We remark that f_0 on the right hand side of Eq. (64) is independent of t, which follows from the orthogonality condition (6). We neglect the higher order terms, $\mathrm{O}(t^2)$, $\mathrm{O}(\beta t)$, etc., in f_F and the macroscopic variables for f_F, i.e. $\boldsymbol{h}_\mathrm{F}$. Then, we have

$$f_\mathrm{F}(t,\boldsymbol{\zeta}) = f_0(s_{j+1/2},0,\boldsymbol{\zeta}) + \beta f_1(s_{j+1/2},0,\boldsymbol{\zeta}) - t\zeta_1 \frac{\partial f_0}{\partial x_1}(s_{j+1/2},0,\boldsymbol{\zeta}), \tag{69}$$

$$\boldsymbol{h}_\mathrm{F} = \boldsymbol{h}_{j+1/2} + t\Delta\boldsymbol{h}, \tag{70}$$

where

$$\boldsymbol{h}_{j+1/2} = \int \boldsymbol{\psi} f_0(s_{j+1/2},0,\boldsymbol{\zeta}) \mathrm{d}\boldsymbol{\zeta}, \tag{71}$$

$$\Delta\boldsymbol{h} = -\int \zeta_1 \boldsymbol{\psi} \frac{\partial f_0}{\partial x_1}(s_{j+1/2},0,\boldsymbol{\zeta}) \mathrm{d}\boldsymbol{\zeta}. \tag{72}$$

The term βf_1 in f_F does not contribute to $\boldsymbol{h}_\mathrm{F}$ because of the orthogonality of f_1. We neglect the higher order terms with respect to t in the local Maxwellian generated from f_F, i.e. $\mathscr{M}(f_\mathrm{F})$. Then, we have

$$\mathscr{M}(f_\mathrm{F}) = f_0(\boldsymbol{h}_{j+1/2},\boldsymbol{\zeta}) + t\frac{\partial f_0}{\partial \boldsymbol{h}}(\boldsymbol{h}_{j+1/2},\boldsymbol{\zeta})\Delta\boldsymbol{h}. \tag{73}$$

From Eqs. (10) and (15), we notice

$$\frac{\partial f_0}{\partial \boldsymbol{h}}\Delta\boldsymbol{h} = -\zeta_1 \frac{\partial f_0}{\partial x_1}(s_{j+1/2},0,\boldsymbol{\zeta}) - \rho_* f_1(s_{j+1/2},0,\boldsymbol{\zeta}). \tag{74}$$

Then, we have

$$f(s_{j+1/2},t,\boldsymbol{\zeta}) = f_0 - t\zeta_1 \frac{\partial f_0}{\partial x_1} + (\beta + \rho_* t)\exp\left(-\frac{\rho_* t}{\epsilon}\right) f_1 - t\rho_* f_1. \tag{75}$$

The solution of the splitting algorithm (75) does not agree with Eq. (20) even if we put $\beta = \epsilon$. Expanding $\exp(-\rho_* t/\epsilon)$ with respect to t under the condition $t \ll \epsilon$, we can enjoy the agreement up to $\mathrm{O}(t)$, as expected from the fact that Eq. (20) is correct up to $\mathrm{O}(t)$ and the result of splitting algorithm without the truncation of higher order terms is correct up to $\mathrm{O}(t^2)$ in this case. For $\epsilon \lesssim t$, however, $\exp(-\rho_* t/\epsilon)$ is considerably different from the approximation by the first few terms in the Taylor expansion; the result of the error analysis of the splitting algorithm [8] does not hold in this case. On the other hand, Strang's splitting, i.e. the free flow step for $t/2$, the collision step for t, and the free flow step for $t/2$, is known as a higher order time integration method for the Boltzmann equation (see [8] for the Boltzmann equation and [3] for general evolutionary equations). Because of the same reason as that for the conventional splitting algorithm, the higher order accuracy is gained only for $t \ll \epsilon$.

Although the difference between Eqs. (20) and (75) is orthogonal to $\boldsymbol{\psi}$, it does not vanish in the numerical flux, since $\int \zeta_1 \boldsymbol{\psi} f_1 \, \mathrm{d}\boldsymbol{\zeta} \neq 0$. Fortunately, we can avoid the error by adjusting the value of β in the following simple way. We require that the resulting numerical flux for Eq. (75) is equal to that for Eq. (20). Then, we have the formula of β,

$$\int_0^{\Delta t} (\beta + \rho_* t) \exp\left(-\frac{\rho_* t}{\epsilon}\right) \mathrm{d}t = \epsilon \Delta t, \tag{76}$$

which is reduced to

$$\beta = \rho_* \Delta t \coth\left(\frac{\rho_* \Delta t}{2\epsilon}\right) - \epsilon. \tag{77}$$

The β is a monotonically increasing function of Δt, $\lim_{\Delta t \to 0} \beta = \epsilon$, and $\beta \sim \rho_* \Delta t$ for $\epsilon \ll \Delta t$.

Let us now consider the extension to the case of Reconstruction-II. Although the contribution of f_1^{II} in the initial condition to the macroscopic variables at the cell-interface is not zero, it is neglected in the following computations as in the case of the GKB scheme. Under this simplification, we have $\rho_* = \rho^{\mathrm{III}}$ and

$$\boldsymbol{h}_{\mathrm{F}} = \boldsymbol{h}_{j+1/2}^{\mathrm{III}} + t \Delta \boldsymbol{h}^{\mathrm{II}}, \tag{78}$$

where

$$\Delta \boldsymbol{h}^{\mathrm{II}} = -\int \zeta_1 \boldsymbol{\psi} \left(\frac{\partial f_0}{\partial x_1}\right)^{\mathrm{II}} \mathrm{d}\boldsymbol{\zeta}. \tag{79}$$

Then, we have

$$\begin{aligned} f(s_{j+1/2}, t, \boldsymbol{\zeta}) = {} & \exp\left(-\frac{\rho^{\mathrm{III}} t}{\epsilon}\right) \left[f_0^{\mathrm{II}} - t \zeta_1 \left(\frac{\partial f_0}{\partial x_1}\right)^{\mathrm{II}} + \beta f_1^{\mathrm{II}} \right] \\ & + \left[1 - \exp\left(-\frac{\rho^{\mathrm{III}} t}{\epsilon}\right)\right] \left[f_0^{\mathrm{III}} + t \frac{\partial f_0}{\partial \boldsymbol{h}} (\boldsymbol{h}_{j+1/2}^{\mathrm{III}}, \boldsymbol{\zeta}) \Delta \boldsymbol{h}^{\mathrm{II}} \right], \end{aligned} \tag{80}$$

where β is determined by Eq. (77) with $\rho_* = \rho^{\mathrm{III}}$. We will call the scheme for Eqs. (80) and (79) Scheme-F.

The numerical flux of Scheme-F is evaluated as

$$\boldsymbol{F}_{\mathrm{F}} \sim \boldsymbol{F}_{\mathrm{D}}, \tag{81}$$

for $\Delta t \ll \epsilon$ and

$$\boldsymbol{F}_{\mathrm{F}} \sim \Delta t \left[\mathscr{F}[f_0^{\mathrm{III}}] + \epsilon \mathscr{F}[f_1^{\mathrm{II}}] \right] + \frac{\Delta t^2}{2} \boldsymbol{K} \Delta \boldsymbol{h}^{\mathrm{II}} + \frac{\epsilon}{\rho^{\mathrm{III}}} \mathscr{F}(f_0^{\mathrm{II}} - f_0^{\mathrm{III}}), \tag{82}$$

for $\epsilon \ll \Delta t$, where $\boldsymbol{K}$ is the same matrix as that defined by Eq. (60). The vector $\boldsymbol{K} \Delta \boldsymbol{h}^{\mathrm{II}}$ corresponds to the numerical flux for $(\partial f_0 / \partial \boldsymbol{h}) \boldsymbol{\Phi}_0 (= -\zeta_1 \partial_{x_1} f_0 - \rho_* f_1)$ as in the case of the GKB scheme, where the corresponding vector is given by $\boldsymbol{K} \Delta \boldsymbol{h}^{\mathrm{III}}$ [see Eq. (59)]. The influence of Reconstruction-II does not survive in the dominant part of the numerical flux $\Delta t \mathscr{F}[f_0]$. Incidentally, the numerical flux of Scheme-F becomes

$$\boldsymbol{F}_{\mathrm{F}} \sim \Delta t \mathscr{F}[f_0^{\mathrm{III}}] + \frac{\Delta t^2}{2} \boldsymbol{K} \Delta \boldsymbol{h}^{\mathrm{II}} + \frac{\epsilon}{\rho^{\mathrm{III}}} \mathscr{F}(f_0^{\mathrm{II}} - f_0^{\mathrm{III}}), \tag{83}$$

without the modification of initial data, i.e. $\beta = \epsilon$. That is, the part of the numerical flux corresponding to the viscous stress and heat flow, $\epsilon \Delta t \mathscr{F}[f_1]$, is canceled out by the error of the splitting algorithm.

The analyses of the GKB scheme, the modified GKB scheme, and Scheme-F for $\epsilon \ll \Delta t$ suggest the following family of kinetic solutions for the numerical flux:

$$f = f_0^{\mathrm{III}} + \epsilon f_1^{\mathrm{a}} - t\zeta_1 \left(\frac{\partial f_0}{\partial x_1} \right)^{\mathrm{b}} - t\rho^{\mathrm{c}} f_1^{\mathrm{c}}, \tag{84}$$

where the superscripts a–c mean the way of reconstruction. In this family, the dominant term f_0 is always approximated by Reconstruction-III. We call the scheme for Eq. (84) with $\mathrm{a} = \mathrm{b} = \mathrm{c} = \mathrm{III}$ Scheme-G, which is the direct extension of Scheme-A to the case of Reconstruction-III. This scheme will be tested together with Scheme-F in Section 4.4.

4.4. Numerical tests of new schemes

In this subsection, we first show the performance of Scheme-F and Scheme-G in the Blasius flow problem. Fig. 8 shows the result of Scheme-F [(120×30) cell system, $\Delta t = 0.01$]. Although the agreement with the exact solution for V is not as good as in the case of Scheme-A (u_2 is of the order of 10^{-3} or 10^{-4} and the discrepancy is magnified considerably in the figure), Scheme-F yields much better results than Scheme-B. Without the modification of the initial data, i.e. $\beta = \epsilon$, the result of Scheme-F becomes very poor (Fig. 9). As mentioned before, the real viscosity is canceled out by the error of the splitting algorithm. This is an example of the boundary-layer made by the numerical viscosity and the numerical boundary-layer is thinner than the physical one. On the other hand, Scheme-G yields excellent results (Fig. 10);

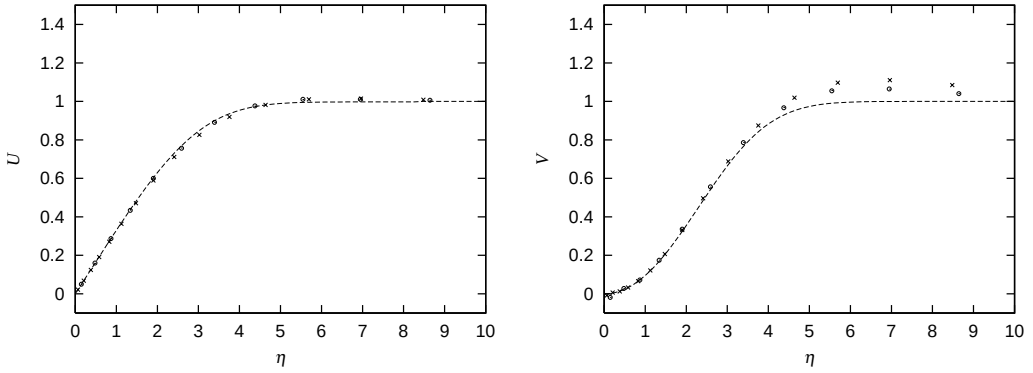

Fig. 8. Blasius flow. The results of Scheme-F for 120×30 cell system and $\Delta t = 0.01$.

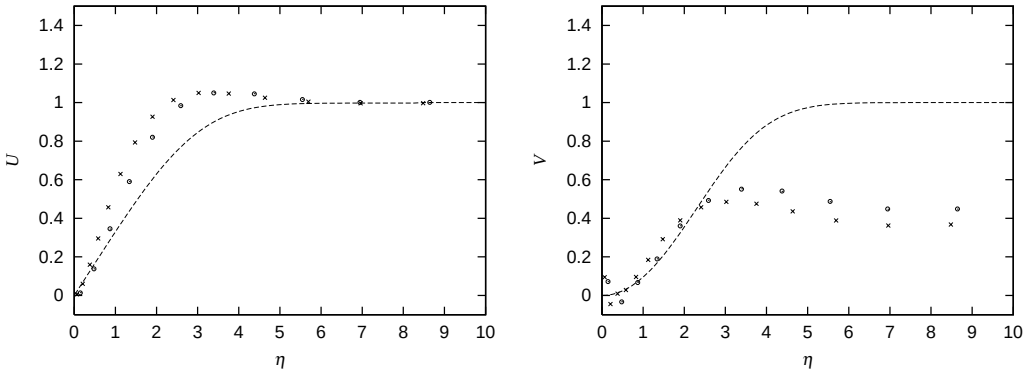

Fig. 9. Blasius flow. The results of Scheme-F ($\beta = \epsilon$) for 120×30 cell system and $\Delta t = 0.01$.

Reconstruction-III becomes nearly identical to Reconstruction-I in this case. Incidentally, it is observed in the case of Scheme-A that the density oscillates slightly in a region between the front of the plate and the upstream boundary (no figure). The amplitude of the oscillations is of the order of 10^{-3}, while the magnitude of ρ is of the order of unity. The amplitude is of the order of 10^{-5} in the case of Scheme-G and no oscillation is observed in the case of Scheme-F. Scheme-E, which inherits the thickest blood of Scheme-A, gives excellent results for U and V and the unfavorable oscillations are almost absent. Presumably, the kinematic dissipation created by Reconstruction-III and the survival of Reconstruction-II, e.g. the last term on the right hand side of Eq. (56), though negligibly small, contribute to the suppression of the small but unfavorable oscillations.

Lastly, we demonstrate the performance of Scheme-F as the Euler solver ($\epsilon = 0$). The results in Sod test case are shown in Fig. 11. Reconstruction-III is created from Reconstruction-II and Van Leer limiter is applied to the slope of Reconstruction-II. Although the shock wave and the contact dis-

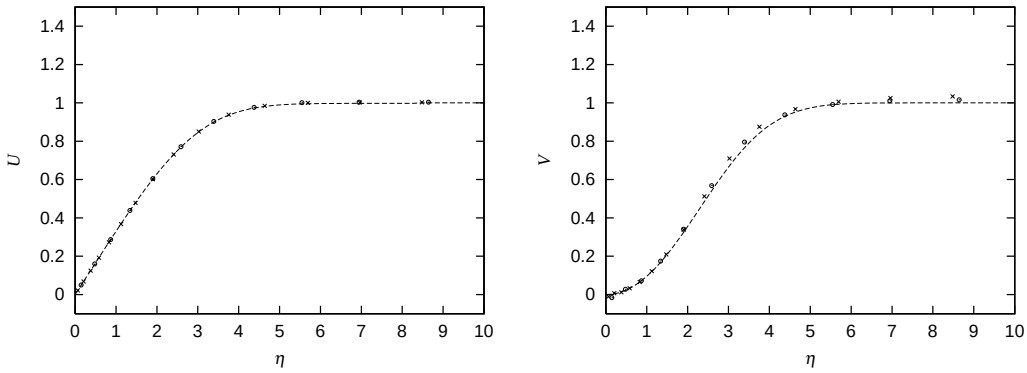

Fig. 10. Blasius flow. The results of Scheme-G for 120×30 cell system and $\Delta t = 0.01$.

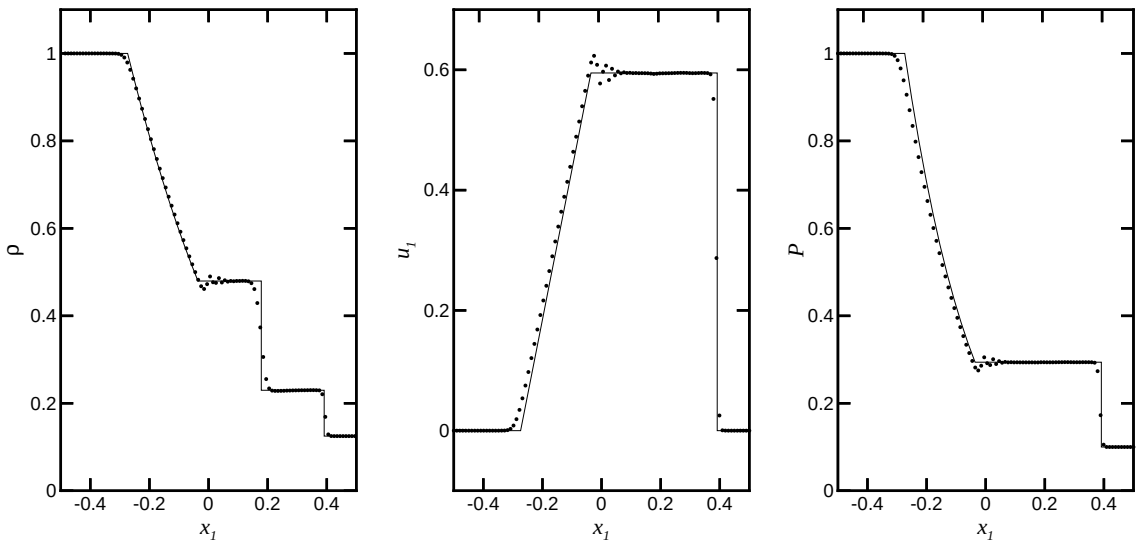

Fig. 11. Sod test case ($t = 0.3$). The solid lines indicate the exact solution and the symbols ● indicate the results of Scheme-F ($\epsilon = 0$) for $\Delta x = 0.01$ (100 cells) and $\Delta t/\Delta x = 0.25$.

continuity are sharply captured without overshoot and undershoot, spurious oscillations are observed around the tail of the expansion wave. Scheme-G and Scheme-F yield almost the same results in this test case. Figs. 12 and 13 show the results in Sjögreen test case and those in Woodward–Colella test

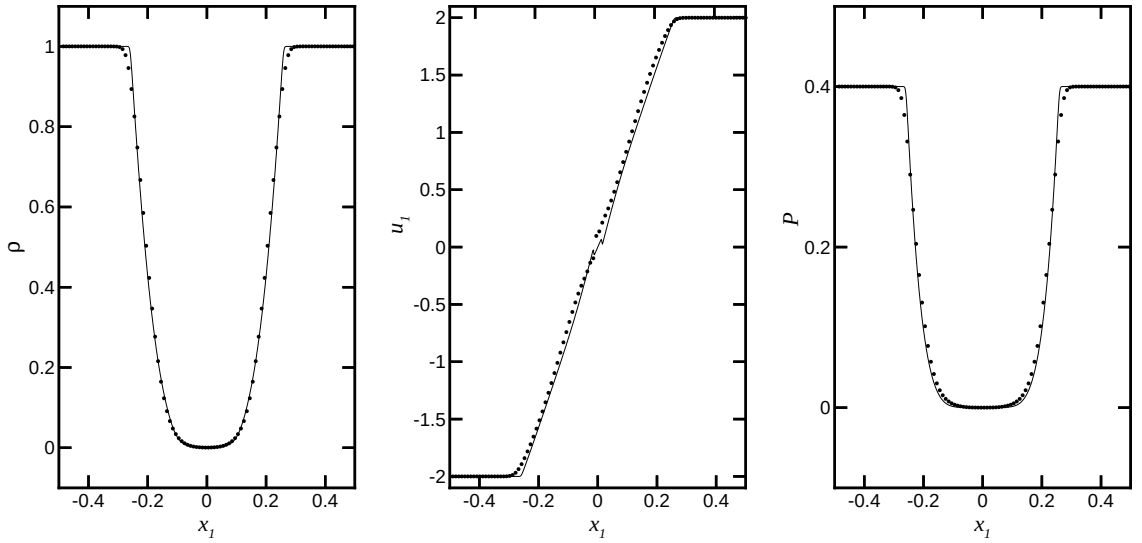

Fig. 12. Sjögreen test case ($t = 0.1$, $\Delta t/\Delta x = 0.25$). The solid lines indicate the results of Scheme-F ($\epsilon = 0$) for $\Delta x = 0.001$ (1000 cells) and the symbols ● indicate those for $\Delta x = 0.01$ (100 cells).

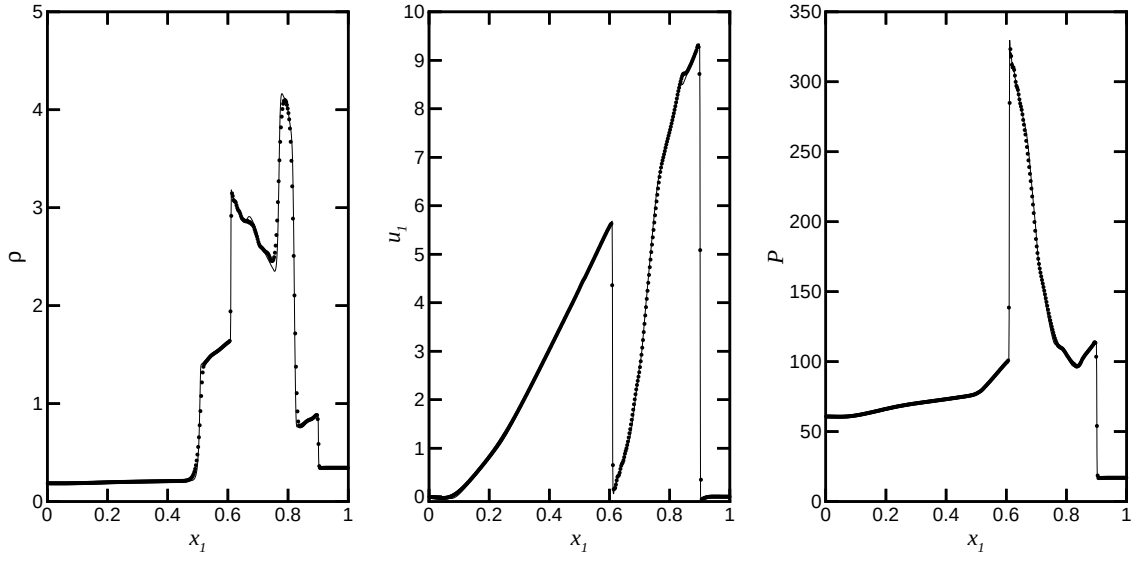

Fig. 13. Woodward–Colella test case ($t = 0.038 \times \sqrt{2}$, $\Delta t/\Delta x = 0.01$). The solid lines indicate the results of Scheme-F ($\epsilon = 0$) for $\Delta x = 0.001$ (1000 cells) and the symbols ● indicate those for $\Delta x = 0.0025$ (400 cells). The factor $\sqrt{2}$ is for the adjustment of time due to the difference of the unit time; the unit time is $L(2RT_0)^{-1/2}$ in the present paper and $L(RT_0)^{-1/2}$ in the literature. The present result is for $\gamma = 5/3$ and the results seen in the literature are for $\gamma = 1.4$.

case, respectively. The results of these test cases for $\gamma = C_p/C_v = 7/5$ are often found in the literature but the present computations are for the case of monatomic gas, i.e. $\gamma = 5/3$. In these test cases, Scheme-F works very well as a robust kinetic scheme. On the other hand, Scheme-G does not work in Sjögreen test case. It works without nonlinear limiter but two small humps appear around both ends of the rarefaction region. If the nonlinear limiter is employed, these humps disappear but the initial crack becomes steeper and the computation finally diverges. So, Scheme-G is excluded from the list of robust kinetic schemes. Incidentally, the computational cost of Scheme-F is almost the same as that of Scheme-B.

4.5. Hybrid scheme

The spurious oscillations observed in Sod test case can be suppressed by increasing the resolution of the cell system or adding small viscosity (e.g. $\epsilon = 0.001$). In the latter case, the shock wave and the contact discontinuity are slightly smeared, however. The improvement can also be brought by modifying Scheme-F in the following way:

$$f(s_{j+1/2}, t, \boldsymbol{\zeta}) = \exp\left(-\frac{\rho^{\mathrm{III}} t}{\epsilon_{\mathrm{c}}}\right)\left[f_0^{\mathrm{II}} - t\zeta_1\left(\frac{\partial f_0}{\partial x_1}\right)^{\mathrm{II}} - \rho^{\mathrm{II}} f_1^{\mathrm{II}}\right] + \epsilon f_1^{\mathrm{a}} + \left[1 - \exp\left(-\frac{\rho^{\mathrm{III}} t}{\epsilon_{\mathrm{c}}}\right)\right]\left[f_0^{\mathrm{III}} + t\frac{\partial f_0}{\partial \boldsymbol{h}}(\boldsymbol{h}_{j+1/2}^{\mathrm{III}}, \boldsymbol{\zeta})\Delta \boldsymbol{h}^{\mathrm{II}}\right], \tag{85}$$

where the superscript 'a' means the reconstruction, i.e. a = I–III, and $\rho^{\mathrm{III}}/\epsilon_{\mathrm{c}}$ should not necessarily be related to the real viscosity, i.e. $\epsilon_{\mathrm{c}} \neq \epsilon$. This is a linear combination of Scheme-B and Scheme-F for $\epsilon = 0$ plus the term ϵf_1, which gives the viscosity and thermal conductivity. The pair of $\exp(-\rho^{\mathrm{III}} t/\epsilon_{\mathrm{c}})$ and $1 - \exp(-\rho^{\mathrm{III}} t/\epsilon_{\mathrm{c}})$ acts as a nonlinear controller; the parameter ϵ_{c} does not have any physical meaning.

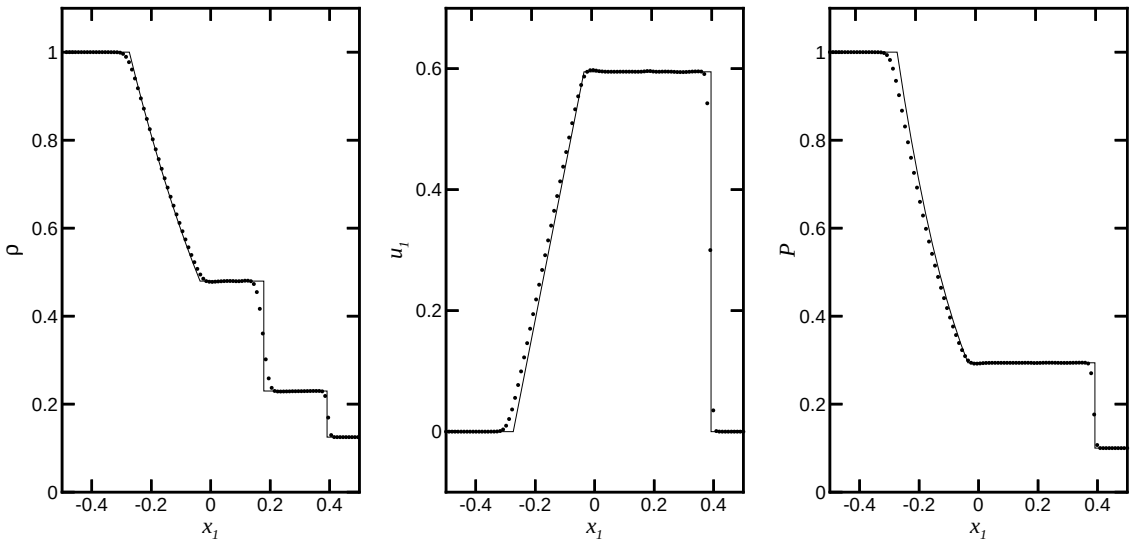

Fig. 14. Sod test case ($t = 0.3$). The solid lines indicate the exact solution and the symbols ● indicate the results of the modified Scheme-F ($\epsilon = 0$ and $\epsilon_{\mathrm{c}} = 0.001$) for $\Delta x = 0.01$ (100 cells) and $\Delta t/\Delta x = 0.25$.

Similar to the actual computation of the GKB scheme, the value of ϵ_c can be determined locally. We call the scheme based on Eq. (85) the modified Scheme-F. The results of the modified Scheme-F for $\epsilon_c = 0.001$ (fixed) and $\epsilon = 0$ in Sod test case are shown in Fig. 14. By blending the numerical flux of Scheme-B slightly, the oscillations around the tail of the expansion wave are suppressed; the shock and contact discontinuities are sharply captured as before. The modified Scheme-F also works very well in the other test cases (no figure).

5. Discussions

In a resolved region, the kinematic dissipation should be equal to or smaller than the dynamical dissipation. It should be sufficiently large in an unresolved region, such as a shock layer, for the suppression of spurious oscillations. Reconstruction-I fulfills only the former requirement and Reconstruction-II fulfills only the latter. Reconstruction-III, which is a continuous reconstruction created from Reconstruction-II, fulfills both of them. Although the initial data is made by Reconstruction-II in the GKB scheme and Scheme-F, the large kinematic dissipation created by Reconstruction-II is avoided by the management of discontinuous reconstruction in their evolution stages.

The importance of management of the discontinuous reconstruction becomes more striking in the steady case. As mentioned in Section 3.2, the result of Scheme-D is almost the same as that of Scheme-B in the Blasius flow problem. While Scheme-B takes account of the derivative of the Maxwellian and the collision effect in the numerical flux, Scheme-D takes account of none of them. The reason for this mysterious reversion is explained as follows. From Eq. (15), we notice that the contribution of these terms to the numerical flux is expressed as

$$-\frac{\Delta t^2}{2}\mathscr{F}\left[\zeta_1\frac{\partial f_0}{\partial x_1}+\rho f_1\right]=\frac{\Delta t^2}{2}\mathscr{F}\left[\frac{\partial f_0}{\partial \boldsymbol{h}}\boldsymbol{\Phi}_0\right]. \tag{86}$$

The $\boldsymbol{\Phi}_0$ is the time derivative corresponding to the Euler equation and it becomes $-\epsilon\boldsymbol{\Phi}_1$ at the steady state, since $\partial \boldsymbol{h}/\partial t = \boldsymbol{\Phi}_0 + \epsilon\boldsymbol{\Phi}_1 = 0$. So, the contribution of these terms reduces to $O(\epsilon\Delta t^2)$; they cancel out each other. This scenario is supported by the agreement between the result of the scheme based on the formula without the derivative and the collision,

$$f = f_0^{\mathrm{III}} + \epsilon f_1^{\mathrm{III}}, \tag{87}$$

and that of Scheme-G; similar to Scheme-G, the scheme based on Eq. (87) yields excellent results in the Blasius flow problem (no figure).

As a promising candidate for the schemes which are robust and accurate for both shock and boundary-layer flows, we finally proposed the modified Scheme-F, Eq. (85), which is a hybrid of two kinetic schemes, Scheme-F and Scheme-B for the compressible Euler equations, plus the viscous term. These kinetic Euler solvers have the common theoretical basis, i.e. the rigorous kinetic equation for the compressible Euler equations derived by the railroad method, i.e. Eq. (17), and consequently, the second order accuracy in time is gained in each scheme. Scheme-B inherits the advantage and disadvantage of the flux vector splitting (FVS) schemes, i.e. the robustness and the excessive numerical dissipation. Scheme-F is regarded as a fortified Lax–Wendroff scheme with the armament of the kinetic continuous reconstruction, which merges the information at both sides of the cell-interface and yields large numerical dissipation in an unresolved region. The less-dissipative nature of Scheme-F in a resolved region is confirmed in the Blasius flow problem and its robustness is demonstrated in the Sjögreen and Woodward–Colella test cases. The drawback of Scheme-F, the spurious oscillations around the tail of the expansion wave found in Sod test case, is overcome by slightly blending the numerical flux of Scheme-B. Scheme-F is not categorized as FVS

and the present hybrid approach is not the improvement of FVS by removing the excessive numerical dissipation, such as EFMO scheme developed by Moschetta and Pullin [6] and AUSMDV scheme developed by Wada and Liou [12].

In the present paper, we consider the kinetic schemes for the compressible NS equations derived from the BGK equation. The viscosity and thermal conductivity in this NS system are proportional to T, while they are proportional to T^s $(1/2 \leqslant s \leqslant 1)$ for the realistic molecular models ($s = 1/2$ for hard-sphere molecules and $s = 1$ for Maxwell molecules). The temperature dependence of these coefficients can easily be adjusted by introducing the temperature dependent collision frequency into the BGK equation; the value of A_c may depend on T. It is well-known, however, that the Prandtl number in the NS system for the BGK equation is equal to unity, while that for the original Boltzmann equation is (exactly or approximately) equal to 2/3. Although the adjustment of Prandtl number can be done at the numerical level (see e.g. [15]), the construction of the kinetic scheme on the basis of the full Boltzmann equation is preferable when we consider the kinetic scheme as a Boltzmann solver for small mean free path; the kinetic scheme and the DSMC are employed as the hybrid approach. There are several ways of the extension to the compressible NS equation for the full Boltzmann equation. The principle of the extension is given by the railroad method for the full Boltzmann equation [10]; f_1 multiplied by ρ in Eq. (20) is left as it is but the one multiplied by ϵ is replaced by f_1 for the Boltzmann equation (the definition of ϵ is also changed).

Acknowledgements

The authors thank to Prof. Kun Xu of Hong Kong University of Science and Technology for his valuable comments and helpful discussions. The present study is supported by Grant-in-aid for Scientific Research No. 14550150 from Japan Society for the Promotion of Science.

References

[1] V.V. Aristov, F.G. Tcheremissine, The kinetic numerical method for rarefied and continuum gas flows, in: O.M. Belotserkovskii, M.N. Kogan, S.S. Kutateladze, A.K. Rebrov (Eds.), Rarefied Gas Dynamics, Plenum Press, New York, 1985, pp. 269–276.
[2] G.A. Bird, Molecular Gas Dynamics and the Direct Simulation of Gas Flows, Oxford University Press, Oxford, 1994; Molecular Gas Dynamics, Oxford University Press, Oxford, 1976.
[3] A.V. Bobylev, T. Ohwada, The error of the splitting scheme for solving evolutionary equations, Appl. Math. Lett. 14 (2001) 45–48.
[4] S.Y. Chou, D. Baganoff, Kinetic flux-vector splitting for the Navier–Stokes equations, J. Comput. Phys. 130 (1997) 217–230.
[5] D. Gilbarg, D.J. Paolucci, The structure of shock waves in the continuum theory of fluids, J. Ration. Mech. Anal. 2 (1953) 617–642.
[6] J.-M. Moschetta, D.I. Pullin, A robust low diffusive kinetic schemes for the Navier–Stokes/Euler equations, J. Comput. Phys. 133 (1997) 193–204.
[7] T. Ohwada, Structure of normal shock waves: direct numerical analysis of the Boltzmann equation for hard-sphere molecules, Phys. Fluids A 5 (1993) 217–234.
[8] T. Ohwada, Higher order approximation methods for the Boltzmann equation, J. Comput. Phys. 139 (1998) 1–14.
[9] T. Ohwada, Boltzmann schemes for the compressible Navier–Stokes equations, in: T.J. Bartel, M. Gallis (Eds.), Rarefied Gas Dynamics, Proceedings of the international symposium on rarefied gas dynamics, 2000, Sydney; AIP Conference Proceedings 585, American Institute of Physics, 2001, pp. 321–328.
[10] T. Ohwada, On the construction of kinetic schemes, J. Comput. Phys. 177 (2002) 156–175.
[11] D.I. Pullin, Direct simulation methods for compressible inviscid ideal gas flow, J. Comput. Phys. 34 (1980) 231–244.
[12] Y. Wada, M.-S. Liou, An accurate and robust flux splitting scheme for shock and contact discontinuities, SIAM J. Sci. Comput. 18 (1997) 633–657.
[13] K. Xu, A new class of gas-kinetic relaxation schemes for the compressible Euler equations, J. Stat. Phys. 81 (1995) 147–164.
[14] K. Xu, Gas-kinetic scheme for unsteady compressible flow simulations, VKI for Fluid Dynamic Lecture Series (1998) 1998–2003.
[15] K. Xu, A gas-kinetic BGK scheme for the Navier–Stokes equations and its connection with artificial dissipation and Godunov method, J. Comput. Phys. 171 (2001) 289–335.